Acta Cryst A FOUNDATIONS ADVANCES

ISSN 2053-2733

Absorption and secondary scattering of X-rays with an off-axis small beam for a cylindrical sample geometry

Daniel C. Van Hoesen,* James C. Bendert and Kenneth F. Kelton

Department of Physics and Institute of Materials Science and Engineering, Washington University, St Louis, MO 63130, USA. *Correspondence e-mail: d.vanhoesen@wustl.edu

Received 10 September 2018
Accepted 14 December 2018

Edited by P. R. Willmott, Swiss Light Source, Switzerland

Keywords: X-ray scattering; cylindrical geometry; absorption; multiple scattering.

Expressions for X-ray absorption and secondary scattering are developed for cylindrical sample geometries. The incident-beam size is assumed to be smaller than the sample and in general directed off-axis onto the cylindrical sample. It is shown that an offset beam has a non-negligible effect on both the absorption and multiple scattering terms, resulting in an asymmetric correction that must be applied to the measured scattering intensities. The integral forms of the corrections are first presented. A small-beam limit is then developed for easier computation.

1. Introduction

Understanding the structure of glasses and liquids, and how that structure changes with temperature and time, is important for understanding processes such as structural relaxation, topological ordering and chemical ordering. The local amorphous structure has also been demonstrated to couple to the crystal nucleation barrier (Kelton *et al.*, 2003; Kelton & Greer, 2010). If the local structures of the liquid or glass and the primary nucleating phase are similar, nucleation will be promoted; if the structures are different it will be inhibited. It has been demonstrated recently that topological ordering in the liquid and glass also couples with the shear viscosity (Iwashita *et al.*, 2013; Soklaski *et al.*, 2016; Mauro *et al.*, 2014; Dai *et al.*, 2018). The subtle changes are small, however, making it essential that X-ray or neutron scattering data be analyzed carefully, taking proper account of sample geometry.

The importance of the effects of absorption and multiple scattering are well known and the general steps to correct scattering experiments have been discussed (Egami & Billinge, 2012; Pauw, 2014). However, the software packages used to process X-ray scattering experiments are not capable of accounting for every geometry and beam parameter. Correction methods for planar geometries have been developed for both transmission and reflection scenarios (Warren & Mozzi, 1966; Dwiggins & Park, 1971; Dwiggins, 1972) as well as for spherical geometries (Dwiggins, 1975*b*; Zeidler, 2012; Bendert *et al.*, 2013). However, samples are often contained in capillaries, requiring correction methods for cylindrical sample geometries. Absorption corrections for this geometry have been developed for several cases, including those when the beam fully encompasses the sample (Paalman & Pings, 1962), the beam has limited width (Kendig & Pings, 1965), for isotropic scattering (Soper & Egelstaff, 1980), and for an inclined beam through an infinite cylinder (Sulyanov *et al.*, 2012); the Paalman & Pings (1962) study is most frequently

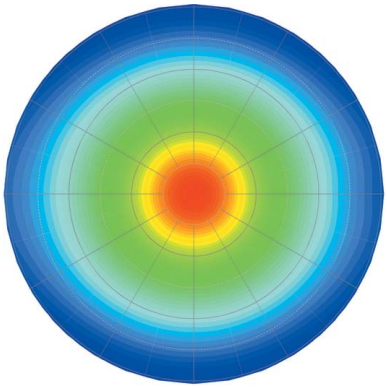

© 2019 International Union of Crystallography

cited. The study by Blech and Averbach is most frequently cited for multiple scattering corrections for cylindrical sample geometries (Blech & Averbach, 1965). However, this article neither considers the realistic case of a finite beam size, or cases where the beam is not centered on the sample. It should also be noted that Monte Carlo integration can be used to account for a wide range of absorption and multiple scattering scenarios, but this method is computationally costly (Seeger, 2003).

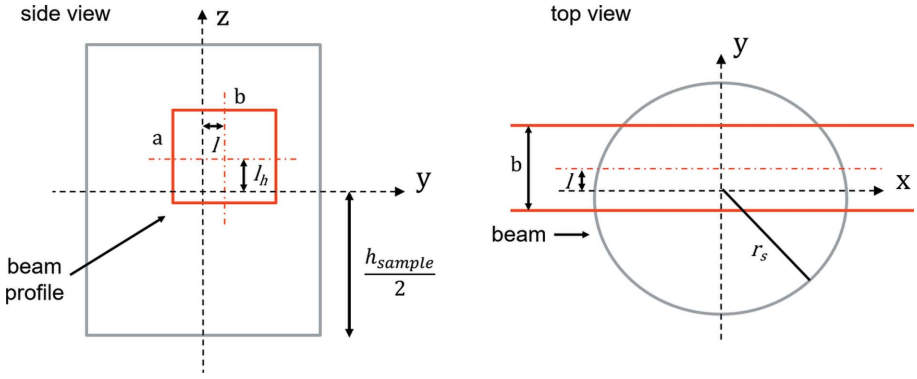

Figure 1
Diagram of the sample geometry and the beam profile.

Here, more generalized expressions for absorption and secondary scattering for a cylindrical sample geometry are given for the two cases when the sample is larger than the beam and the beam is transmitted through the sample off-center from the cylindrical axis. This development follows earlier work for the case of spherical amorphous samples with an off-axis beam (Bendert *et al.*, 2013).

2. Theory

While the introductory theory for absorption and multiple scattering of a generalized geometry and material is described elsewhere (Bendert *et al.*, 2013), a few concepts are reviewed for reference. The infinitesimal scattered intensity, dI, at a distance r from the scattering volume, dV, is given by

$$\mathrm{d}I(r, 2\theta, \phi) = I_0\left(\frac{\sigma_e n}{r^2}\right)P(\kappa_0, 2\theta, \phi)J(2\theta)\mathrm{d}V, \qquad (1)$$

where σ_e is the differential Thomson scattering cross section for electrons, n is the number density of the scattering sample, $P(\kappa_0, 2\theta, \phi)$ accounts for polarization effects and $J(2\theta)$ is the first-order approximation to the scattering intensity. The intensities of both the incident and scattered beams are attenuated on passing through the sample according to Beer's law, $I(r) = I_0\exp(-\mu r)$, which must be considered in the integration of equation (1). The experimentally measured intensities are, therefore, multiplied by an absorption correction factor V/V', where V is the volume of intersection between the beam and the sample and V' $[= \int\int\int \exp(-\mu r)\mathrm{d}V]$ is the effective volume of intersection between the beam and the sample. Elastic scattering is assumed, *i.e.* there is no change in μ for the scattered beam.

Secondary scattering is also considered in the form of a multiplicative factor, $(1 + I_2/I_1)^{-1}$, where I_1 is the intensity of the beam after a single scattering event and I_2 is the intensity of the beam after the second scattering event. While there are actually multiple scattering events, the probability of these becomes significantly less, so only secondary scattering need be considered as a correction. Multiplying the sum of scattering events, $I_1 + I_2$, by the factor above recovers the primary scattering intensity, I_1. Integrating equation (1) for the first scattering event, considering the attenuated scattering volume, gives

$$I_1 = \frac{I_0\sigma_e n}{r^2}P(\kappa_0, 2\theta, \phi)J(2\theta)V'. \qquad (2)$$

2.1. Absorption correction

Assume a rectangular beam of height a and width b intersecting a cylindrical sample (Fig. 1), with the center of the beam offset from the center of the cylinder by a distance l in the y direction and a distance l_h in the z direction.

Consider first a cylinder of infinite height. When the beam profile does not encounter the top and bottom of the cylinder the intersection volume is

$$V = \int_{l_h-\frac{a}{2}}^{l_h+\frac{a}{2}}\mathrm{d}z\int_{-\left(\frac{b}{2}-l\right)}^{\frac{b}{2}+l}\mathrm{d}y\int_{-(r_s^2-y^2)^{1/2}}^{(r_s^2-y^2)^{1/2}}\mathrm{d}x. \qquad (3)$$

The effective intersection volume, considering attenuation of the beam, is

$$V' = \int_{l_h-\frac{a}{2}}^{l_h+\frac{a}{2}}\mathrm{d}z\int_{-\left(\frac{b}{2}-l\right)}^{\frac{b}{2}+l}\mathrm{d}y\int_{-(r_s^2-y^2)^{1/2}}^{(r_s^2-y^2)^{1/2}}\mathrm{d}x \times \exp\left\{-\mu\left[(r_s^2-y^2)^{1/2} + x + R(2\theta, \phi, x, y, z)\right]\right\}. \qquad (4)$$

The beam first travels a distance $(r_s^2 - y^2)^{1/2} + x$ in the x direction before a scattering event at the point (x_0, y_0, z_0). The beam then travels an additional $R(2\theta, \phi, x_0, y_0, z_0)$ distance to the edge of the cylinder, causing the detection of an event on the detector at 2θ and ϕ. Similar to the method of Sulyanov *et al.* (2012), the value for R is calculated by constraining spherical coordinates to the edge of the cylinder. Edge points on the cylinder are given by

$$\begin{aligned} x_e &= x_0 + R\cos(2\theta) \\ y_e &= y_0 + R\sin(2\theta)\cos(\phi) \\ z_e &= z_0 + R\sin(2\theta)\sin(\phi). \end{aligned} \qquad (5)$$

R is found by constraining the equations by $r_s^2 = x_e^2 + y_e^2$,

$$R = \Big(-[x_0\cos(2\theta) + y_0 p] + \big\{[x_0\cos(2\theta) + y_0 p]^2 - (x_0^2 + y_0^2 - r_s^2)[\cos(2\theta)^2 + p^2]\big\}^{1/2}\Big) / [\cos(2\theta)^2 + p^2], \quad (6)$$

where $p = \sin(2\theta)\cos(\phi)$. For a cylinder of finite height, there are cases when the scattered beam exits the top or bottom of the cylinder, as shown in Fig. 2. For this case, the value of R from equation (6) will be for point (x', y', z') outside the sample instead of (x_e, y_e, z_e) (see Fig. 2). For correctly accounting for sample absorption, R is constrained between the values $h_{\rm sample}/2 = z_0 + R\sin(2\theta)\sin(\phi)$ and $-h_{\rm sample}/2 = z_0 + R\sin(2\theta)\sin(\phi)$. Also, from equation (6), R becomes infinite if $\cos(2\theta)^2 + p^2 = 0$, since the beam is scattered in the $\pm z$ direction. For this case, R becomes equal to the distance from z_0 to the top or bottom of the cylinder.

Taking account of these points the scattered beam path, $R(2\theta, \phi, x_0, y_0, z_0, h_{\rm sample})$, for a finite cylinder is

$$R = \begin{cases} \dfrac{-[x_0\cos(2\theta)+y_0p]+\left\{[x_0\cos(2\theta)+y_0p]^2-(x_0^2+y_0^2-r_s^2)[\cos(2\theta)^2+p^2]\right\}^{1/2}}{\cos(2\theta)^2+p^2} \\ \quad \text{for } -\dfrac{h_{\rm sample}}{2} < z_e < \dfrac{h_{\rm sample}}{2} \\ \dfrac{\frac{h_{\rm sample}}{2}-z_0}{\sin(2\theta)\sin(\phi)} \text{ for } z_e > \dfrac{h_{\rm sample}}{2} \\ -\dfrac{\frac{h_{\rm sample}}{2}+z_0}{\sin(2\theta)\sin(\phi)} \text{ for } z_e < -\dfrac{h_{\rm sample}}{2}. \end{cases} \quad (7)$$

For faster computation, the attenuated volume integration [equations (3) and (4)] can be simplified in the small-beam limit. Two of the three integrals in equation (4) are reduced, giving the effective scattering volume as

$$V' = ab\int_{-(r_s^2-l^2)^{1/2}}^{(r_s^2-l^2)^{1/2}} \mathrm{d}x \times \exp\big\{-\mu\big[(r_s^2 - l^2)^{1/2} + x + R(2\theta, \phi, x, l, l_h)\big]\big\}. \quad (8)$$

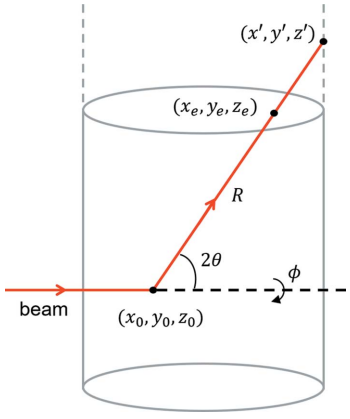

Figure 2
Scattering event at point (x_0, y_0, z_0) inside the cylindrical sample leading to the beam cylinder wall intersection at point (x', y', z') above the cylinder. The distance the beam travels inside the sample is the distance from point (x_0, y_0, z_0) to point (x_e, y_e, z_e).

As $2\theta \to 0$, for $-h_{\rm sample}/2 < z_e < h_{\rm sample}/2$, and $a, b \to 0$ the asymptotic calculation reduces significantly and can be expressed in terms of unitless sample fractions, $l_s = l/r_s$, $x_s = x/r_s$, $R_s = R/r_s$ and μr_s. The effective scattering volume is then

$$V' = abr_s \exp\big[-\mu r_s(1 - l_s^2)^{1/2}\big] \int_{-(1-l_s^2)^{1/2}}^{(1-l_s^2)^{1/2}} \mathrm{d}x_s \times \exp\big\{-\mu r_s[x_s + R_s(2\theta, \phi, x_s)]\big\}, \quad (9)$$

where

$$R_s = \Big(-[x_s\cos(2\theta) + l_s p] + \big\{[x_s\cos(2\theta) + l_s p]^2 - (x_s^2 + l_s^2 - 1)[\cos(2\theta)^2 + p^2]\big\}^{1/2}\Big) / [\cos(2\theta)^2 + p^2]. \quad (10)$$

For $V = 2abr_s$, the asymptotic expansion of the off-axis absorption correction (V/V') is

$$\frac{V}{V'} \simeq \frac{\exp\big[2\mu r_s(1 - l_s^2)^{1/2}\big]}{(1 - l_s^2)^{1/2}} \times \sum_{i=0}^{\infty} A_i(\mu r_s, l_s, \phi)(2\theta)^i, \quad (11)$$

with the first five coefficients listed in Table 1. Equation (8) is easily solved when $z_e < -h_{\rm sample}/2$ and $h_{\rm sample}/2 < z_e$, because R takes on the much simpler form as shown above. It is important to note that, in the small-beam limit, at $\phi = 0$ and $\phi = \pi$ the cylindrical absorption correction is equivalent to the spherical absorption correction derived earlier (Bendert *et al.*, 2013).

2.2. Secondary scattering correction

The path steps for the beam in the sample when multiple scattering is considered are listed below and illustrated in Fig. 3.

(i) Beam enters the sample traveling in the x direction.

(ii) Beam scatters at point (x_0, y_0, z_0) with scattering angles $2\theta_1$ and ϕ_1.

(iii) Beam travels distance r_1 to point (x_1, y_1, z_1).

(iv) Beam scatters at point (x_1, y_1, z_1) with scattering angles $2\theta_2$ and ϕ_2.

(v) Beam travels distance $R(2\theta, \phi, x_1, y_1, z_1)$ to the sample edge at point (x_e, y_e, z_e).

When the detector is far from the sample, the three sets of scattering angles are related by a $2\theta_1$ rotation about the z axis and a ϕ_1 rotation about the x axis. These are found given a point on the detector $(2\theta, \phi)$ and the first scattering angles $2\theta_1$ and ϕ_1 (Bendert *et al.*, 2013).

Equation (1) only considers the first scattering event. The infinitesimal scattering intensity of the second event is

$$\mathrm{d}I_2 = \frac{I_0 n^2 \sigma_e^2}{r_1^2 r_2^2} P(\kappa_0, 2\theta_1, \phi_1) J(2\theta_1) P(\kappa_1, 2\theta_2, \phi_2) J(2\theta_2) \times \exp\big[-\mu(r_1 + r_2)\big]\mathrm{d}V_1\mathrm{d}V_2. \quad (12)$$

This must be integrated over two volumes. The first is the volume intersection of the beam with the sample. The second

Table 1
Coefficients for the expansion of the cylindrical absorption correction.

i	A_i
0	1
1	$-\mu r_s l_s \cos(\phi)$
2	$\frac{-\mu r_s}{6(l_s^2-1)}\left[-2\mu r_s l_s^4\cos(\phi)^2+2\mu r_s l_s^2\cos(\phi)^2+6(1-l_s^2)^{1/2}l_s^2\cos(\phi)^2-3(1-l_s^2)^{1/2}l_s^2-4(1-l_s^2)^{1/2}\cos(\phi)^2+3(1-l_s^2)^{1/2}\right]$
3	$\frac{\mu r_s l_s\cos(\phi)}{6(l_s^2-1)}\left[4\mu r_s l_s^2\cos(\phi)^2(1-l_s^2)^{1/2}+6l_s^2\cos(\phi)^2-2\mu r_s(1-l_s^2)^{1/2}l_s^2-5l_s^2+2\mu r_s(1-l_s^2)^{1/2}-2\mu r_s(1-l_s^2)^{1/2}\cos(\phi)^2+5-6\cos(\phi)^2\right]$
4	$\frac{-\mu r_s}{360(l_s^2-1)}\left[8(\mu r_s)^3 l_s^6\cos(\phi)^4+30\mu r_s l_s^4-320\mu r_s l_s^4\cos(\phi)^2-8(\mu r_s)^3 l_s^4\cos(\phi)^4+360\mu r_s l_s^4\cos(\phi)^4-75(1-l_s^2)^{1/2}l_s^2+32(\mu r_s)^2 l_s^2\cos(\phi)^4(1-l_s^2)^{1/2}-60\mu r_s l_s^2-360(1-l_s^2)^{1/2}\cos(\phi)^4 l_s^2+420(1-l_s^2)^{1/2}l_s^2\cos(\phi)^2-336\mu r_s l_s^2\cos(\phi)^4+380\mu r_s l_s^2\cos(\phi)^2+75(1-l_s^2)^{1/2}+216(1-l_s^2)^{1/2}\cos(\phi)^4-60\mu r_s\cos(\phi)^2+30\mu r_s+16\mu r_s\cos(\phi)^4-280(1-l_s^2)^{1/2}\cos(\phi)^2\right]$
5	$\frac{-\mu r_s l_s\cos(\phi)}{360(l_s^2-1)}\left[-16(\mu r_s)^3 l_s^4\cos(\phi)^2(1-l_s^2)^{1/2}+32(\mu r_s)^3 l_s^4\cos(\phi)^4(1-l_s^2)^{1/2}+480\mu r_s l_s^2\cos(\phi)^4(1-l_s^2)^{1/2}-88(\mu r_s)^2 l_s^2\cos(\phi)^4-24(\mu r_s)^3 l_s^2\cos(\phi)^4(1-l_s^2)^{1/2}+32(\mu r_s)^2 l_s^2\cos(\phi)^2+16(\mu r_s)^3 l_s^2\cos(\phi)^2(1-l_s^2)^{1/2}+360\cos(\phi)^4 l_s^2+183l_s^2+150\mu r_s(1-l_s^2)^{1/2}l_s^2-540l_s^2\cos(\phi)^2-600\mu r_s l_s^2\cos(\phi)^2(1-l_s^2)^{1/2}-183+540\cos(\phi)^2+348\mu r_s(1-l_s^2)^{1/2}\cos(\phi)^2+48(\mu r_s)^2\cos(\phi)^4-150\mu r_s(1-l_s^2)^{1/2}-192\mu r_s\cos(\phi)^4(1-l_s^2)^{1/2}-360\cos(\phi)^4-32(\mu r_s)^2\cos(\phi)^2\right]$

is the volume of the cone produced by the first scattering event, defined by sweeping out the angles $2\theta_1$ and ϕ_1. It is important to note that the polarization changes after the first scattering event giving $P(\kappa_1, 2\theta_2, \phi_2)$ (see Bendert *et al.*, 2013). The first volume is given in equation (4). The second volume is

$$V_2 = \int_0^{\pi} \sin(2\theta_1)\,\mathrm{d}2\theta_1 \int_0^{2\pi} \mathrm{d}\phi_1 \int_0^{R(2\theta_1,\phi_1,x,y,z)} r_1^2\,\mathrm{d}r_1. \qquad (13)$$

Integrating equation (12),

$$I_2 = \frac{I_0 n^2 \sigma_e^2}{r^2} \int_{l_h-\frac{a}{2}}^{l_h+\frac{a}{2}} \mathrm{d}z \int_{-\left(\frac{b}{2}+l\right)}^{\frac{b}{2}-l} \mathrm{d}y \int_{-(r_s^2-y^2)^{1/2}}^{(r_s^2-y^2)^{1/2}} \mathrm{d}x \times \int_0^{\pi} \sin(2\theta_1)\,\mathrm{d}2\theta_1 \int_0^{2\pi} \mathrm{d}\phi_1 \int_0^{R(2\theta_1,\phi_1,x,y,z)} \mathrm{d}r_1 \times P(\kappa_0, 2\theta_1, \phi_1) J(2\theta_1) P(\kappa_1, 2\theta_2, \phi_2) J(2\theta_2) \times \exp\left\{-\mu\left[x + (r_s^2 - y^2)^{1/2} + r_1 + R(2\theta, \phi, x_1, y_1, z_1)\right]\right\}, \qquad (14)$$

where r_1 defines the distance from the first scattering point to the second scattering point, and the bound on r_1 is defined by the distance from the first scattering point to the edge of the sample. The positions x_1, y_1 and z_1 are given by

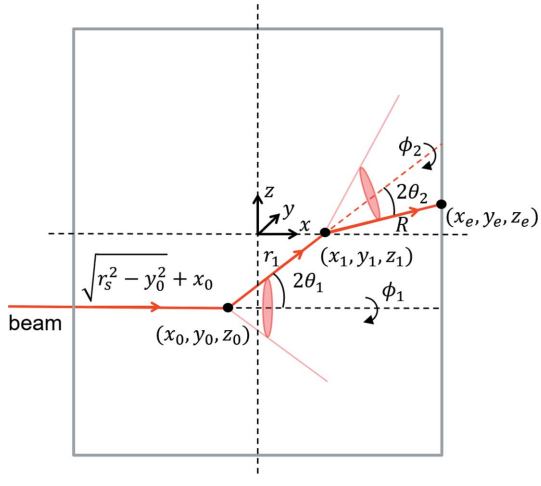

Figure 3
Multiple scattering steps showing two scattering events.

$$x_1 = x_0 + r_1\cos(2\theta_1)$$
$$y_1 = y_0 + r_1\sin(2\theta_1)\cos(\phi_1)$$
$$z_1 = z_0 + r_1\sin(2\theta_1)\sin(\phi_1). \quad (15)$$

The self-scattering intensity is used for $J(2\theta)$ here. Additional approximations and discussions of the accuracy for $J(2\theta)$ are summarized elsewhere (Warren & Mozzi, 1966; Dwiggins, 1972; Bendert *et al.*, 2013; Malet *et al.*, 1973). While the secondary scattering correction is complete with I_2/I_1, it is computationally expensive to solve the integrals required to find I_2. If we again take the small-beam limit, equation (14) becomes

$$I_2 = \frac{I_0 n^2 \sigma_e^2 ab}{r^2} \int_{-(r_s^2-l^2)^{1/2}}^{(r_s^2-l^2)^{1/2}} \mathrm{d}x \int_0^{\pi} \sin(2\theta_1)\,\mathrm{d}2\theta_1 \int_0^{2\pi} \mathrm{d}\phi_1 \times \int_0^{R(2\theta_1,\phi_1,x,l,h_{\rm beam})} \mathrm{d}r_1 \times P(\kappa_0, 2\theta_1, \phi_1)J(2\theta_1)P(\kappa_1, 2\theta_2, \phi_2)J(2\theta_2) \times \exp\left\{-\mu\left[x + (r_s^2 - l^2)^{1/2} + r_1 + R(2\theta, \phi, x_1, y_1, z_1)\right]\right\}, \quad (16)$$

and a simpler approximation results,

$$\frac{I_2}{I_1} = \frac{n\sigma_e V}{2r_s P(\kappa_0, 2\theta, \phi)J(2\theta, \phi)V'} \int_{-(r_s^2-l^2)^{1/2}}^{(r_s^2-l^2)^{1/2}} \mathrm{d}x \times \int_0^{\pi} \sin(2\theta_1)\,\mathrm{d}2\theta_1 \int_0^{2\pi} \mathrm{d}\phi_1 \int_0^{R(2\theta_1,\phi_1,x,l,h_{\rm beam})} \mathrm{d}r_1 \times P(\kappa_0, 2\theta_1, \phi_1)J(2\theta_1)P(\kappa_1, 2\theta_2, \phi_2)J(2\theta_2) \times \exp\left\{-\mu\left[x + (r_s^2 - l^2)^{1/2} + r_1 + R(2\theta, \phi, x_1, y_1, z_1)\right]\right\}. \quad (17)$$

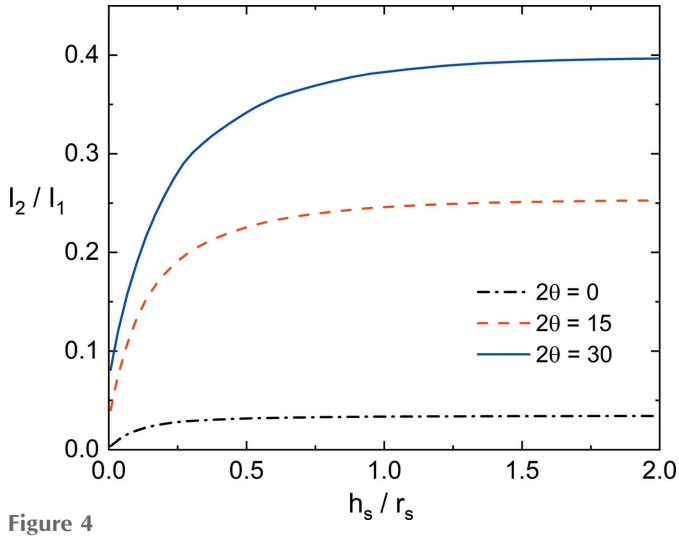

Figure 4
Dependence of the cylinder height on secondary scattering intensity for Au at multiple 2θ angles with $2\mu r_s = 10$, $l_s = 0$, λ = 0.1 Å and $\phi = 0$.

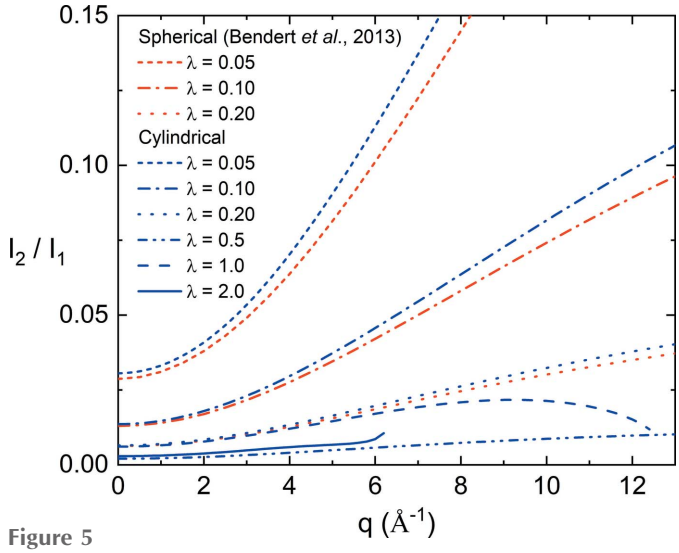

Figure 5
Comparison of secondary scattering correction as a function of q and beam wavelength for cylindrical and spherical geometries for a Zr sample with $2\mu r_s = 1$, $l_s = 0$ and $\phi = 0$.

3. Results and discussion

Three elements, Au, Zr and Si, which have dramatically different attenuation coefficients, are selected to illustrate the results of absorption and multiple scattering of a small beam for a cylindrical sample geometry. A non-polarized beam ($\kappa_0 = 0$) is assumed for the calculations. Fig. 4 shows the dependence of the sample height on secondary scattering (I_2/I_1) from an Au sample as a function of the ratio of cylinder height to radius (h_s/r_s). It is assumed for these calculations that the incident beam has no offset ($l_s = 0$) and that $\phi = 0$. As observed, the effect of the sample height only becomes significant when the radius of the sample becomes larger than the height. The following discussions will focus on the case when the height of the cylinder is significantly larger than the radius as is the case for most X-ray experiments.

The attenuation coefficient is strongly dependent on the energy of the incident photons. The changes in the multiple scattering correction in the cylindrical Zr sample for several values of the wavelength of the incident beam are shown in Fig. 5. They are compared with the result for a spherical sample, using the corrections developed by Bendert *et al.* (2013). Low-energy photons have a small multiple scattering correction and cannot probe large q ranges. For λ = 2.0 Å the maximum q is 2πÅ^{-1} as shown below.

The absorption corrections for cylindrical and spherical samples of Au, Zr and Si, at $\phi = 0$ detector location, are shown in Fig. 6. The absorption correction is normalized by $\exp(-2\mu r_s)$. It is not surprising that in the small-beam limit the absorption corrections for spherical and cylindrical samples at $\phi = 0$ are equivalent (Fig. 6), since there the curvature of the cylinder matches the curvature of the sphere This is shown by setting ϕ to zero in equation (11) and in equation (19) in Bendert *et al.* (2013). There are differences in the secondary

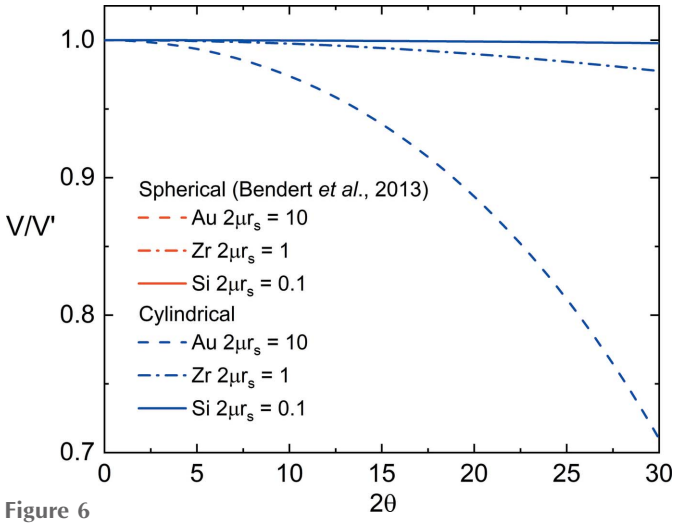

Figure 6
Comparison of spherical and cylindrical absorption corrections for three different test cases with $l_s = 0$ and $\phi = 0$.

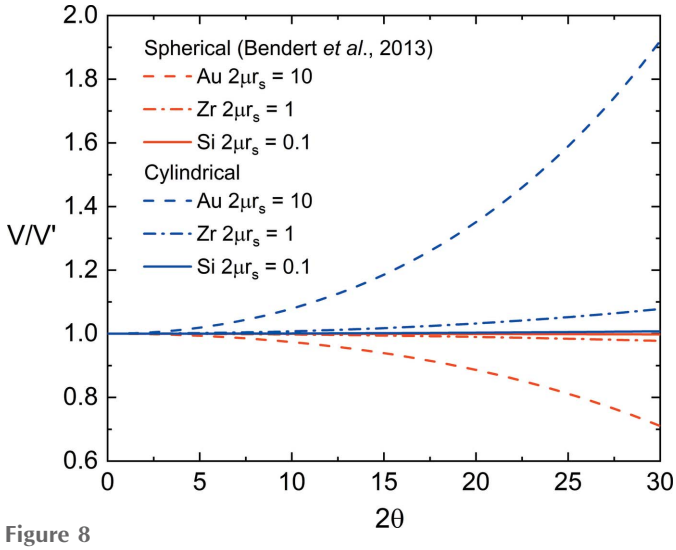

Figure 8
Comparison of spherical and cylindrical absorption corrections for three different test cases with $l_s = 0$ and $\phi = \pi/2$.

scattering corrections, however, because the beam can travel in the z direction after the first scattering event. The small differences in multiple scattering corrections are shown in Fig. 5 and can also be seen in Bendert *et al.* (2013) (Fig. 6*b*).

In the cylindrical geometry at the $\phi = \pi/2$ detector position, the distance that the beam travels through the sample for $2\theta > 0$ or $2\theta < 0$, $d_{2\theta}$, is greater than the distance traveled when the incident beam is normal to the surface of the sample, d_0 (Fig. 7). There is then a greater attenuation, with V/V' increasing with increasing magnitude of 2θ. The opposite is true for the spherical geometry ($d_0 < d_{2\theta}$), with V/V' decreasing as 2θ deviates from 0. These trends are shown in Figs. 8 and 12.

The incident beam may not be aligned with the center of the cylinder; if this is the case, it is important to account for the offset, l. The offset can be characterized by a comparison with the radius of the sample, r_s. Let $l_s = l/r_s$ be the metric for the beam offset. Figs. 9 and 10 show the 2D detector asymmetric absorption and the asymmetric secondary scattering corrections as a function of 2θ and ϕ for a test sample of Au for four different offsets. Fig. 11 shows line profiles of Figs. 9 and 10 at $\phi = 0$. The $l_s = 0$ case is the same as the case when $2\mu r_s = 10$ in Fig. 6. Absorption corrections can be dramatically asymmetric if the beam center is far from the cylinder center. Additionally, asymmetry from the off-axis scattering beam creates an asymmetry in the secondary scattering correction. As expected, the zero offset, $l_s = 0$, case is symmetric about $2\theta = 0$ and the curves become more asymmetric as the beam offset increases. Again, it is shown that for absorption the spherical and cylindrical cases are equivalent for $\phi = 0$. Fig. 12 shows asymmetric absorption and the asymmetric secondary

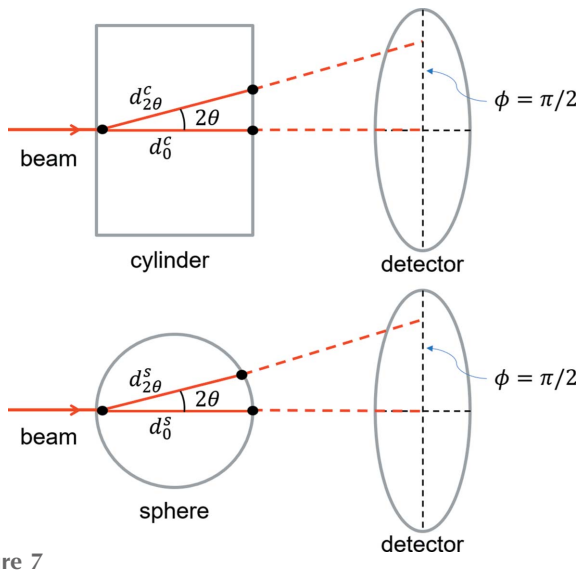

Figure 7
The difference between the absorption correction for cylindrical and spherical geometries at $\phi = \pi/2$. In the cylindrical geometry $d^c_0 < d^c_{2\theta}$; however, in the spherical geometry $d^s_0 > d^s_{2\theta}$.

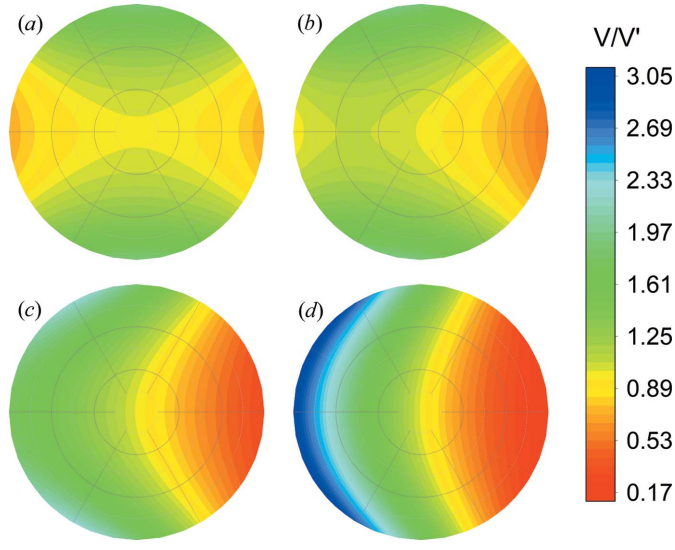

Figure 9
Asymmetric detector image for the absorption correction with offset distance (*a*) $l_s = 0$, (*b*) $l_s = 0.1$, (*c*) $l_s = 0.3$ and (*d*) $l_s = 0.5$ for a test sample with $2\mu r_s = 10$.

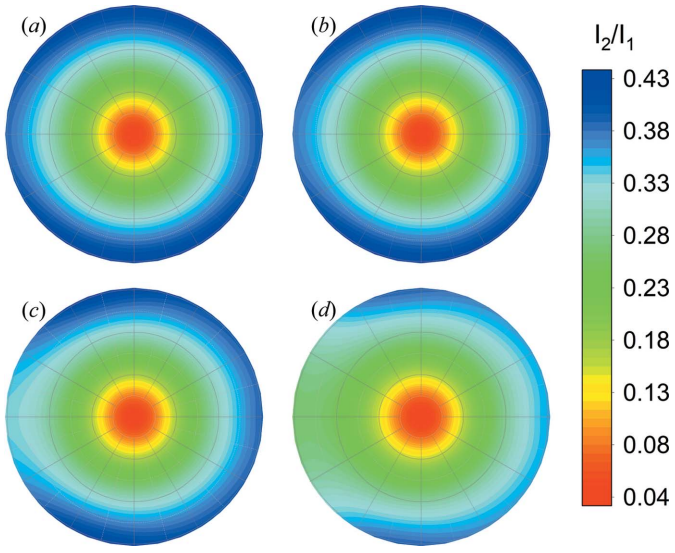

Figure 10
Asymmetric detector image for the multiple scattering correction with offset distance (*a*) $l_s = 0$, (*b*) $l_s = 0.1$, (*c*) $l_s = 0.3$ and (*d*) $l_s = 0.5$ for an Au test sample with $2\mu r_s = 10$ and $\lambda = 0.1$ Å.

scattering correction line profiles of Figs. 9 and 10 for the Au test sample when $\phi = \pi/2$. For this case, there is a difference in the absorption corrections for spherical and cylindrical geometries because of the surface curvature differences between spheres and cylinders, as mentioned above.

4. Conclusions

Correctly accounting for absorption and secondary scattering is critical for obtaining accurate results from scattering data, particularly when the changes in structure that are investigated are small. Building on the work of others for absorption (Paalman & Pings, 1962; Dwiggins, 1972, 1975*a*) and secondary scattering (Warren & Mozzi, 1966; Dwiggins & Park, 1971), corrections for scattering from samples with cylindrical geometries were developed. Accounting for the position of the beam on the sample is also important. For spherical samples, offsets in the position of the beam from the center of the sample produce significant asymmetries in the signal measured at the detector (Bendert *et al.*, 2013). These effects were examined here for cylindrical samples.

The conditions for the corrections presented here go beyond the previous work for cases where the beam fully encompasses the sample (Blech & Averbach, 1965) or for beam widths smaller than the cylinder diameter (Soper & Egelstaff, 1980). Soper and Egelstaff used a method of concentric rings to calculate the beam path length inside the sample, assuming that the beam height is the same as the sample height. Although the case of an off-axis beam with a beam height smaller than the sample height and associated beam path lengths for a cylindrical geometry were mentioned by Soper and Egelstaff, they were not computed. The work presented here develops a generalized, user-friendly method for calculating the multiple scattering and absorption corrections, taking account of the beam profile and position on the sample. The solutions for absorption and multiple scattering are in terms of 2θ and ϕ, the 2D detector coordinates, implying that the corrections may be useful for samples producing anisotropic scattering patterns in addition to isotropic scatterers. The exact expressions obtained, expressed in integral form, can be solved using current computer resources. Some approximations were also made to reduce the number of integrals, expressions that can be used to obtain results more quickly from simple numerical integration.

Funding information

The following funding is acknowledged: National Science Foundation (grant No. DMR 17-20296).

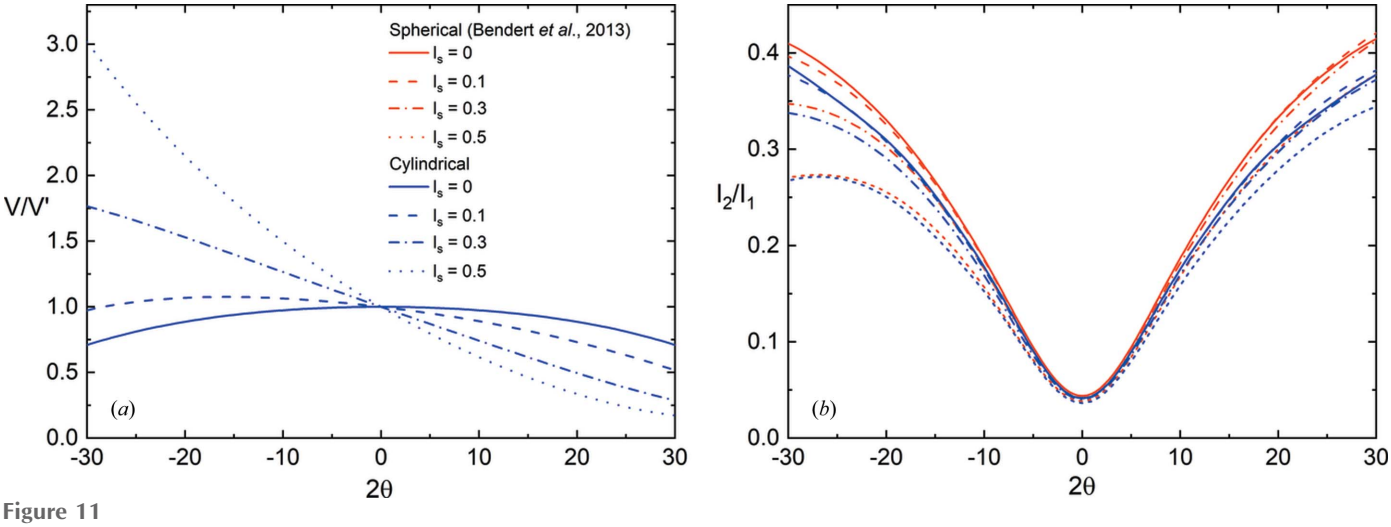

Figure 11
Asymmetric (*a*) absorption and (*b*) multiple scattering corrections for a line profile across the $\phi = 0$ axis with offset distances $l_s = 0, 0.1, 0.3$ and 0.5 for an Au test sample with $2\mu r_s = 10$ and $\lambda = 0.1$ Å.

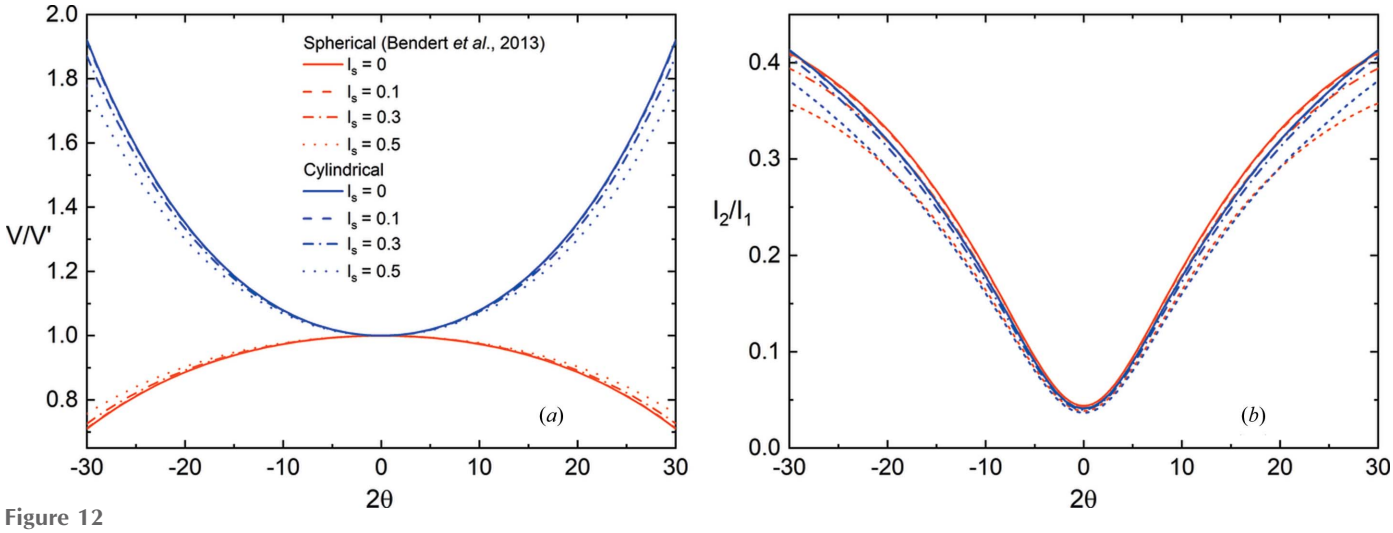

Figure 12
Asymmetric (*a*) absorption and (*b*) multiple scattering corrections for a line profile across the $\phi = \pi/2$ axis with offset distances $l_s = 0, 0.1, 0.3$ and 0.5 for an Au test sample with $2\mu r_s = 10$ and $\lambda = 0.1$ Å.

References

Bendert, J. C., Blodgett, M. E. & Kelton, K. F. (2013). *Acta Cryst.* A**69**, 131–139.
Blech, I. A. & Averbach, B. L. (1965). *Phys. Rev.* **137**, A1113–A1116.
Dai, R., Ashcraft, R. & Kelton, K. F. (2018). *J. Chem. Phys.* **148**, 204502.
Dwiggins, C. W. (1972). *Acta Cryst.* A**28**, 158–163.
Dwiggins, C. W. (1975*a*). *Acta Cryst.* A**31**, 146–148.
Dwiggins, C. W. (1975*b*). *Acta Cryst.* A**31**, 395–396.
Dwiggins, C. W. & Park, D. A. (1971). *Acta Cryst.* A**27**, 264–272.
Egami, T. & Billinge, S. J. L. (2012). *Underneath the Bragg Peaks: Structural Analysis of Complex Materials*. *Pergamon Materials Series*, Vol. 16, 2nd ed. Oxford: Pergamon.
Iwashita, T., Nicholson, D. M. & Egami, T. (2013). *Phys. Rev. Lett.* **110**, 1–5.
Kelton, K. F. & Greer, A. L. (2010). *Nucleation in Condensed Matter – Applications in Materials and Biology*. Amsterdam: Elsevier.
Kelton, K. F., Lee, G. W., Gangopadhyay, A. K., Hyers, R. W., Rathz, T. J., Rogers, J. R., Robinson, M. B. & Robinson, D. S. (2003). *Phys. Rev. Lett.* **90**, 195504.
Kendig, A. P. & Pings, C. J. (1965). *J. Appl. Phys.* **36**, 1692–1698.
Malet, G., Cabos, C., Escande, A. & Delord, P. (1973). *J. Appl. Cryst.* **6**, 139–144.
Mauro, N. A., Blodgett, M., Johnson, M. L., Vogt, A. J. & Kelton, K. F. (2014). *Nat. Commun.* **5**, 4616.
Paalman, H. H. & Pings, C. J. (1962). *J. Appl. Phys.* **33**, 2635–2639.
Pauw, B. R. (2014). *J. Phys. Condens. Matter*, **25**, 383201.
Seeger, P. A. (2003). *Nucl. Instrum. Methods Phys. Res. A*, **510**, 290–299.
Soklaski, R., Tran, V., Nussinov, Z., Kelton, K. F. & Yang, L. (2016). *Philos. Mag.* **96**, 1212–1227.
Soper, A. K. & Egelstaff, P. A. (1980). *Nucl. Instrum. Methods*, **178**, 415–425.
Sulyanov, S., Gogin, A. & Boysen, H. (2012). *J. Appl. Cryst.* **45**, 93–97.
Warren, B. E. & Mozzi, R. L. (1966). *Acta Cryst.* **21**, 459–461.
Zeidler, A. (2012). *J. Appl. Cryst.* **45**, 122–123.